The Role of Small-Scale Vortices in Enhancing Surface Winds and Damage in Hurricane Harvey (2017)

JOSHUA WURMAN AND KAREN KOSIBA

Center for Severe Weather Research, Boulder, Colorado

(Manuscript received 6 November 2017, in final form 6 January 2018)

ABSTRACT

Strong hurricanes cause severe, but highly variable, wind damage to homes and community infrastructure. It has been speculated, but not previously shown, that damage variability is caused by tornadoes or other small-scale phenomena. Here, the authors present the first mapping and tracking of persistent tornado-scale vortices (TSVs) in the eyewall and the first documentation of the likely role of eyewall mesovortices (MVs) and TSVs in enhancing surface winds and damage. Unprecedented finescale observations in the eyewall of Hurricane Harvey (2017) were obtained by a Doppler on Wheels (DOW) radar deployed inside the eye. These observations reveal several persistent eyewall MVs revolving about the eye, as well as superimposed subkilometer-scale TSVs. Wind field perturbations associated with TSVs and MVs are less than those typical in supercell tornadoes, but since they are embedded in strong background eyewall flow, they are likely responsible for the enhancement of surface wind gusts and significant damage, including destroyed buildings and lofted vehicles. Potential climate change may result in more frequent intense and/or rapidly intensifying hurricanes; thus, understanding and forecasting the causes of hurricane wind damage is a high priority.

1. Introduction

Hurricane winds cause direct harm to people, infrastructure, and communities (Irfan 2017; Dapena et al. 2017). Significant variability in damage patterns has been noted in intense hurricanes, and it has been speculated that these may result from the passage of tornadoes, downbursts, and/or eyewall mesovortices (MVs) (Fujita 1992; Wakimoto and Black 1994; Stewart and Lyons 1996; Willoughby and Black 1996). Climate change could lead to an increase in the frequency of intense hurricanes (Knutson et al. 2010), and rapid intensification immediately before landfall may become more likely (Emanuel 2017). Since wind damage can have severe and long-lasting effects on infrastructure (Dapena et al. 2017), better understanding of the nature of these hazards, leading to better prediction and design for resiliency, is critical. But, to date, only a few studies have compared wind data from finescale mobile radar observations to wind data obtained from near-surface anemometer observations, and those studies have focused on the role of hurricane boundary layer (HBL) rolls (Lorsolo et al. 2008; Kosiba et al. 2013).

The HBL exhibits linearly organized coherent structures known as HBL rolls (HBLRs) (Wurman and Winslow 1998; Morrison et al. 2005; Foster 2005). HBLRs, aligned roughly with the background wind direction with cross-flow wavelengths of 300–1000 m, are associated with wind field perturbations of 5–10 $m\,s^{-1}$ above the background wind speed (Wurman and Winslow 1998; Lorsolo et al. 2008; Kosiba and Wurman 2010; Kosiba et al. 2013). The role of HBLRs in enhancing turbulent kinetic energy and fluxes of energy and momentum, which may influence hurricane intensification, has been explored (Lorsolo et al. 2010; Rogers et al. 2012; Kosiba and Wurman 2014). Numerical simulations suggest kilometer-sized HBLRs may contribute to regions of enhanced surface winds (Zhu 2008). Rare real-time observations of specific progressive building failures have been linked to individual and multiple HBLR passages (Kosiba and Wurman 2010). However, since HBLRs are not anchored geographically, extending many kilometers, many locations near the eyewall passage experience wind perturbations from

Denotes content that is immediately available upon publication as open access.

Supplemental information related to this paper is available at the Journals Online website: https://doi.org/10.1175/MWR-D-17-0327.s1.

Corresponding author: Joshua Wurman, jwurman@cswr.org

DOI: 10.1175/MWR-D-17-0327.1

several to many HBLRs. In the absence of real-time documentation, damage is only diagnosed by post-event aerial and ground-based surveys. The result of multiple roll crossings is the conflation of many individual damage swaths, effectively delocalizing and smoothing damage patterns. Additionally, varying construction standards and building component responses to wind duration/direction complicate wind speed estimates (e.g., Edwards et al. 2013). MVs, few- to several-kilometer-scale vortices embedded within the hurricane eyewall, may impact hurricane damage potential and intensity (Willoughby and Black 1996; Kossin and Schubert 2004; Montgomery et al. 2006; Corbosiero et al. 2006; Marks et al. 2008; Reasor et al. 2009; Kosiba and Wurman 2010; Hendricks et al. 2012; Wingo and Knupp 2016). Idealized numerical and laboratory simulations of MVs indicate that strongly rotating flows could maintain these coherent structures for several revolutions about the main vortex (Kossin and Schubert 2001; Montgomery et al. 2002).

More recently, intense winds measured by dropsondes were speculated to be linked to <4-km-scale vortices along the inner eyewall (Aberson et al. 2006; Stern et al. 2016). But the limited sampling inherent to dropsondes, the lack of very finescale radar mapping, and the lack of ground verification precluded diagnosing the structure of the phenomena or impacts on the surface wind field. Surface anemometers have measured wind gusts in many landfalling hurricanes (e.g., Schroeder et al. 2002; Schroeder and Smith 2003; Masters et al. 2010; Lorsolo et al. 2008; Kosiba et al. 2013; Giammanco et al. 2016; Krupar et al. 2016). However, specific intense gusts observed in hurricanes have not been linked previously to finely mapped atmospheric phenomena, such as tornado-scale vortices (TSVs).

2. Deployment in Hurricane Harvey

A Doppler on Wheels (DOW) mobile radar (Wurman et al. 1997; CSWR 2017) and other Center for Severe Weather Research (CSWR) instrumentation were deployed inside the eye of category 4 Hurricane Harvey as it made landfall along the Texas coast around 0300 UTC 26 August 2017. This deployment permitted the mapping, in unprecedented detail, of eyewall MVs, HBLRs, and, for the first time, embedded persistent TSVs, a distinctly different phenomenon from supercell-generated tornadic vortices. The DOW was deployed at the Aransas County/Rockport Airport. Two pod weather stations were deployed at the airport, and two were deployed on an elevated bridge across the channel between the Copano and Aransas Bays (Fig. 1). The DOW site was next to a runway, with the closest obstructions (low buildings and trees) 350–500 m upstream (to the north). The DOW, with a 0.95° beamwidth, conducted

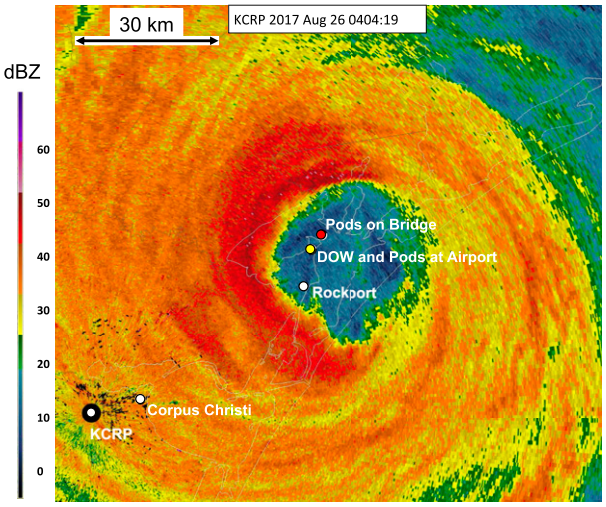

FIG. 1. DOW and pod deployment as Hurricane Harvey makes landfall near Rockport, TX. Radar reflectivity measured by the National Weather Service KCRP radar at 0404:19 UTC 26 Aug 2017 showing the eyewall of Harvey just after landfall. DOW, pod, KCRP, and city locations are shown.

near-surface, approximately 1°-elevation surveillance scans every 9–12 s during the hurricane landfall. A 250-kW magnetron transmitter produced 0.167- and 0.333-μs pulses at 9.450 GHz. Received signals were downconverted and sampled at 3–12 MHz to produce raw complex time series data with range gates of 12.5–50 m, integrated into beams every 0.5°. The transmitter produced pulses at staggered frequency combinations of 2250/3000 and 3000/4000 Hz. An R.M. Young 05103 blade anemometer, recording at 1 Hz, was raised over the DOW to 8 m above ground level (AGL). Intense winds, measured at up to 65 m s^{-1} by the anemometer, precluded reliable radar scanning during the inner eyewall passage. As local winds decreased as the eye began to pass over the DOW, scanning resumed. Airborne debris from damaged buildings north of the airport destroyed the instruments on two of the pods. Intense winds and/or airborne debris pushed two pods off the bridge into the sea; only one was recovered.

DOW data, DOW-mounted anemometer data, and aerial and ground-based imagery were combined to quantify directly the effects of the TSVs and MVs on surface winds and damage.

3. Eyewall mesovortices enhance surface winds

Observations from the DOW and the proximate National Weather Service radar (KCRP) revealed the motion, structure, and evolution of MVs revolving around the eye (Fig. 2). MVs were persistent and were tracked for more than one revolution about the eye, tracing quasi-trochoidal, looping, ground-relative paths (Fig. 3). High-temporal-frequency,

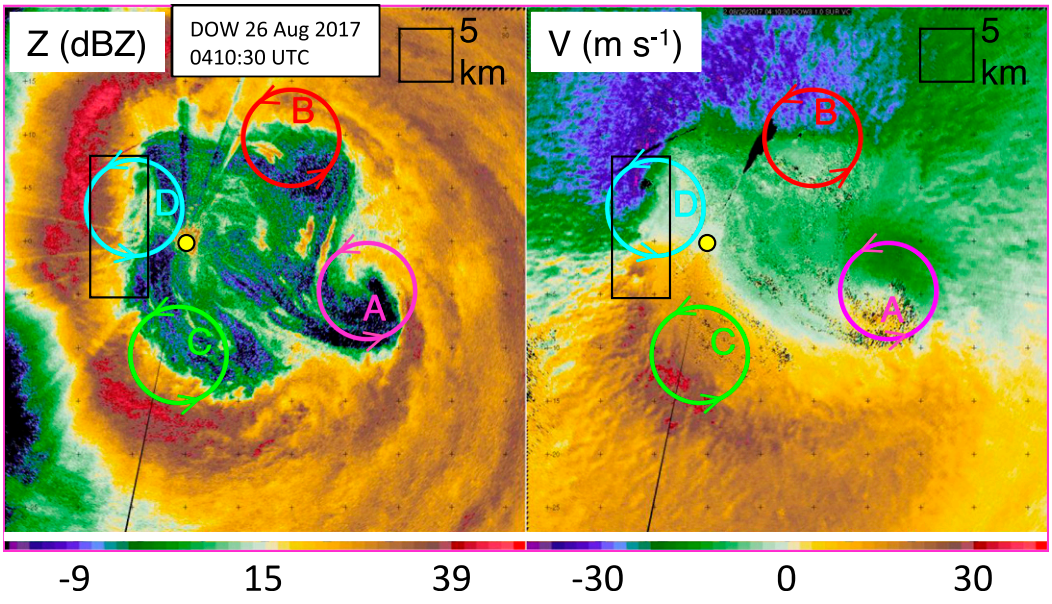

FIG. 2. Finescale DOW radar imagery of hurricane eye and eyewall, including four MVs. (left) Radar reflectivity and (right) Doppler velocity measured from inside eye (DOW location indicated with yellow dot) at 0410:30 UTC 26 Aug 2017. Four MVs revolving about the eye are highlighted schematically with colored circles. Black rectangle is zoomed-in area shown in Fig. 6.

finescale-spatial-resolution DOW data permitted detailed tracking of individual MVs. The diameters, defined as the distance between maximum wind field perturbations of each MV, ranged from 2 to 11 km, with the amplitude of the wind speed perturbations typically ± 15–$20\,m\,s^{-1}$ above/below background eyewall wind speeds. Pronounced convergent Doppler signatures were evident at times in MVs B and D. MV eye-relative rotational speed averaged approximately $32\,m\,s^{-1}$, substantially slower than the ~ 55–$70\,m\,s^{-1}$ background eyewall wind speeds (the DOW and KCRP measured winds aloft of up to $\sim 70\,m\,s^{-1}$), indicating substantial upstream propagation speed consistent with the MVs being vortex Rossby waves (Montgomery and Kallenbach 1997) [and analogous to the propagation of similar vortices observed in tornadoes; Wurman (2002)]. The revolution period for individual MVs around the eye averaged 2200 s. The slow, $2.5\,m\,s^{-1}$, north-northwestward translation of the eye meant that many locations were impacted by more than one MV. Since there were four MVs, the average recurrence interval over specific eye-center relative locations was approximately 2200/4 = 550 s. KCRP measured MV centers crossing near or over the DOW at approximately 0239, 0249, 0300, 0308, 0319, and 0329 UTC, with an average interval of 600 s. MV centers were scanned by KCRP only every 150 s, so these crossing times are approximate.

The DOW anemometer measured a peak wind of $65\,m\,s^{-1}$ ($60\,m\,s^{-1}$ 3-s moving average, not shown; all averages herein are moving averages) during eyewall passage (Fig. 4). Using a roughness length $z_0 = 0.03$ m, typical for open exposure "airport runway," and a standard boundary layer wind profile (Wieringa et al. 2001; Kosiba et al. 2013), the calculated peak 1-s wind gust at 10 m AGL was $68\,m\,s^{-1}$ ($62\,m\,s^{-1}$ 3-s average). Since the upstream terrain was rougher about 2.5 km north of the DOW, and then marine farther upstream, gust factor analysis (Fig. 5) comparing the DOW anemometer time series during the 50-min eyewall passage with those of Durst (1960) and Schroeder et al. (2002) was conducted. The magnitude of the short-period gusts, compared to the longer-term average wind speed, suggests that the effective exposure was between "open," with $z_0 \sim 0.02$–0.05 m, and "open to roughly open," with $z_0 \sim 0.05$–0.09 m (Schroeder et al. 2002). Using $z_0 \sim 0.05$ m results in peak 10-m AGL wind gusts of $68\,m\,s^{-1}$ ($63\,m\,s^{-1}$ 3-s average). The timing of peaks in the smoothed wind speed time series (0238, 0249, 0301, 0308, and 0317 UTC) is coincident with the passage of MVs over the DOW. Wind speed enhancement was most pronounced at 0238 and 0249 UTC when MV centers passed a few kilometers southeast of the DOW, exposing the DOW to the maximum wind field perturbations, near their radius of maximum winds, where their northerly direction wind perturbations were nearly directly additive to the northerly background eyewall wind. The MV crossing the DOW at about 0300 UTC was less organized and did not result in much wind speed enhancement. MVs with centers passing nearly over the DOW at later times exposed the anemometer to maximum wind speed perturbations before and after

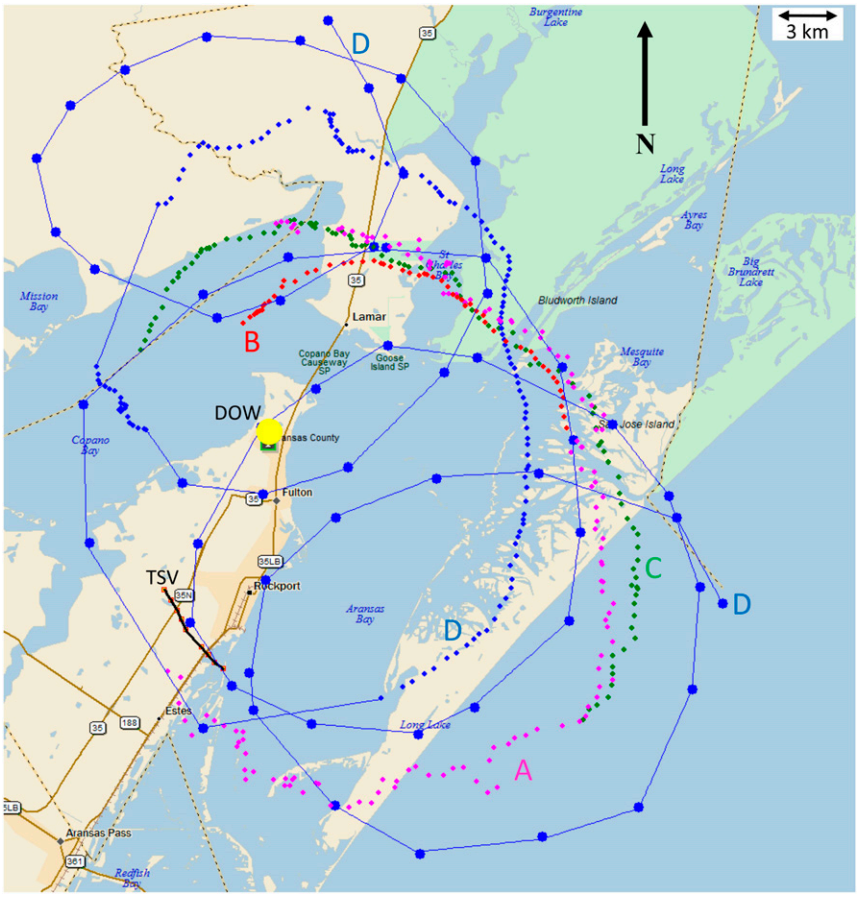

FIG. 3. Spiral, quasi-trochoidal, looping paths of the eyewall MVs and track of an intense TSV. The approximate tracks of the MV centers as measured by the DOW are shown with dots, color-coded as in Fig. 2 to delineate different MVs. One MV track outside the DOW observation period from KCRP data (large dots/line) is shown. The track of the TSV causing damage, with implied near-surface winds over 50 m s^{-1}, is indicated with the black line. Yellow dot is DOW site.

center passages, with perturbations at significant angles to the background flow, complicating comparison with anemometer measurements. Fourier spectral analysis (Fig. 5) (NCAR 2018) of the anemometer data revealed a strong peak at 600 s caused by the passage of MVs crossing at the same interval. These data and analysis represent the first direct evidence of MVs enhancing measured surface winds.

4. Tornado-scale vortices enhance violence of winds

Very-fine-spatiotemporal-scale, within-eye DOW observations permitted the mapping and tracking of hurricane eyewall TSVs (Fig. 6). TSVs were common in the western eyewall, both within and between MVs, but were not clearly visible in much coarser KCRP data. They appear to have formed in the northern eyewall and dissipated as they revolved west, south, and southeast of the hurricane center. Wind speed perturbations were typically ±10–20 m s^{-1}. A DOW-based climatology indicated that the average supercell tornado wind speed perturbation is ~30 m s^{-1} (Alexander and Wurman 2008), and a ±20 m s^{-1} wind speed perturbation is the minimum threshold usually applied for DOW-detected tornadoes (Wurman and Kosiba 2013). TSV wind speed perturbations are substantially weaker. TSVs were typically trackable for 60–240 s over distances of up to 11 km. While the short duration of trackability may suggest a shorter lifetime than is typical for supercell tornadoes (Alexander and Wurman 2008), the start and end times of these weaker TSVs are somewhat subjective, and there is no established minimum intensity threshold. Some of the observed TSVs were in pairs/groups/clusters oriented quasi perpendicularly to the background wind, resulting in apparent waves of TSVs

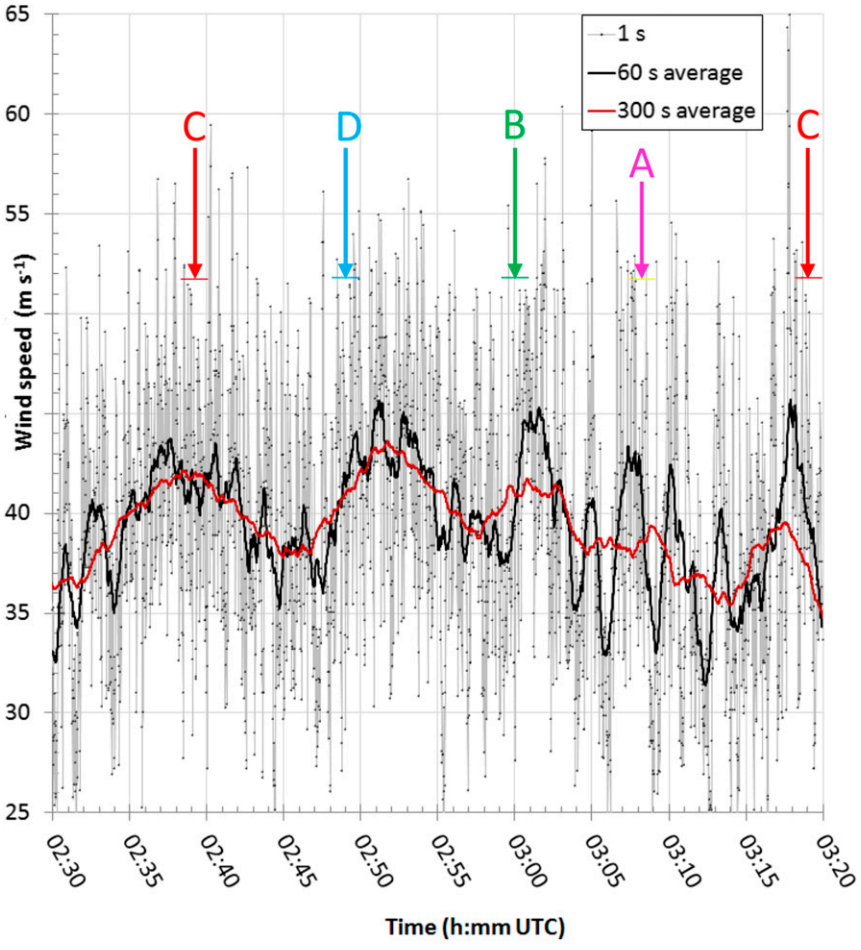

FIG. 4. Winds observed by DOW-mounted anemometer during eyewall passage in time and spectral domain. Time history of wind speeds measured by DOW-mounted anemometer 8 m AGL showing quasi-periodic maxima approximately every 600 s and gusts up to 65 m s^{-1}. Closest approach times of MVs indicated with colored arrows corresponding to colored circles in Fig. 2. MV center passages to the southeast of the DOW are most clearly associated with enhanced wind speeds at 0239 and 0249 UTC.

with a typical spacing between waves of ~2.5–4.5 km. Weak perturbations in the reflectivity field with ~2–4-km spacing were visible in DOW and KCRP data. Wavelike structures near the inner eyewall with ~2-km spacing have been produced numerically (Ito et al. 2017). The 3–5-km periodicity noted in photographic and radar observations of inner eyewall cloud features (Bluestein and Marks 1987) may have been associated with similar TSVs. Dropsonde observations (Aberson et al. 2006; Stern et al. 2016) have likely sampled TSVs. TSVs are distinct from minisupercell-spawned tornadoes occurring in the outer rainbands of some hurricanes (Spratt et al. 1997; McCaul et al. 2004) and are not associated with supercell thunderstorms.

While the wind speed perturbations associated with the TSVs are small, compared to those typical for supercell tornadoes, TSV winds are superimposed on the already intense background eyewall flow and/or perturbations resulting from eyewall MVs. Thus, the resulting damage potential is substantially higher than that associated with the background wind speed. DOW-anemometer wind speeds average 40 m s^{-1} during the 3000 s centered on eyewall passage. During MV passages, 60-s averaged winds increase a few meters per second to 43–46 m s^{-1}. During TSV passages, wind gusts increase to 55–65 m s^{-1} (3-s average gusts increase to 50–60 m s^{-1}), depending on whether the TSVs are embedded in or between MVs.

While the DOW was unable to scan from 0203 to 0356 UTC, during the passage of the most intense portion of the eyewall, observations shortly thereafter permit the measurement of the near-DOW TSV propagation speed

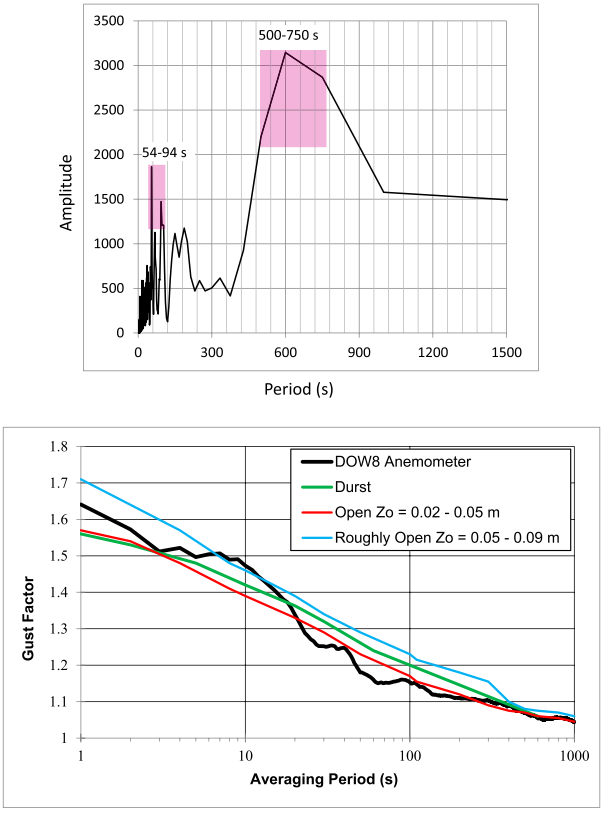

FIG. 5. Analysis of winds observed by DOW-mounted anemometer during eyewall passage in time and spectral domain. (top) Fourier spectral analysis of the wind data time series reveals strong peaks at 600 and 54–94 s caused by the passage of MVs and TSVs. (bottom) Gust factor analysis of wind time series, compared to those observed in different exposures (Schroeder et al. 2002; Durst 1960) reveals gusts consistent with roughness length $z_0 \sim 0.05$ m and enhanced short-period gustiness at averaging times $\leq$3 s, consistent with the rapid passage of small TSVs.

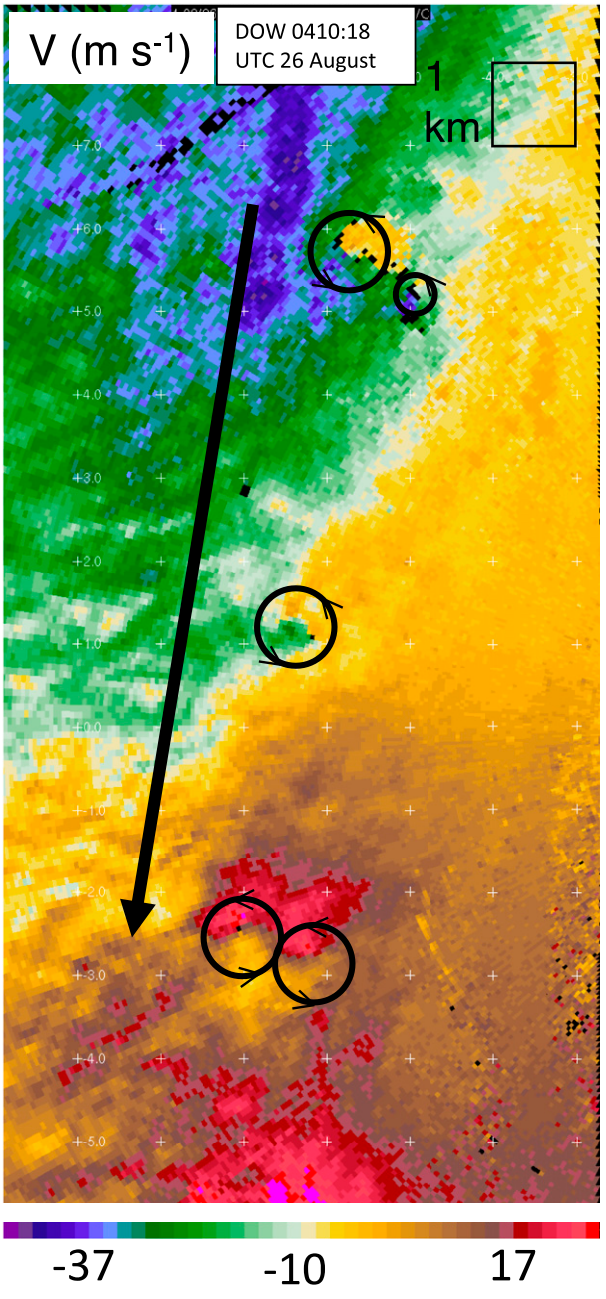

FIG. 6. DOW Doppler velocity in hurricane eyewall TSVs. DOW-measured Doppler velocity at 0410:18 UTC 26 Aug 2017 reveals single and paired TSVs (demarked schematically with black circles) translating rapidly southward in the northwestern eyewall embedded in the strong northerly flow in the eyewall (black arrow).

(51 m s^{-1}) and inter-TSV spacing (2.5–4.5 km), with a recurrence interval of ~50–90 s. Spectral analysis of the DOW anemometer time series reveals that in addition to the ~600-s period caused by MVs, there are prominent modes at 54 and 94 s, likely caused by the passage of TSVs (Fig. 5). This is the first time that TSV structures have been linked directly to enhanced measured surface winds.

TSVs cause much shorter-duration enhanced winds than most supercell-spawned tornadoes due to their ~50 m s^{-1} translation speed. Measured winds 10 m s^{-1} or more than the 60-s average centered on the peak gust at the DOW persist just 9 s. The gust factor analysis (Fig. 5) reveals a slope steeper than expected for $z_0 \sim 0.05$ at averaging intervals $\leq$3 s, consistent with the very rapid 50 m s^{-1} passage of small regions, $O(100)$ m, of maximum winds associated with individual TSVs. Typical durations of enhanced winds measured in supercell tornadoes by in situ anemometers (Wurman et al. 2013) and radar (Lee and Wurman 2005; Wurman et al. 2007, 2013, 2014) are $O(30)$ s. While there are no supporting full-scale engineering analyses, the duration of intense winds likely affects damage potential (Wurman et al. 2014), and the effects of long-duration gustiness on structures in

hurricanes have been documented in real time (e.g., Kosiba and Wurman 2010).

5. Tornado-scale vortices and damage

Hurricane landfall occurred over a region comprising ocean bays and diverse land use, including broad undeveloped areas, residential areas (containing both manufactured and conventional houses), farms, industrial areas, and towns. The slow translation speed of the hurricane meant that some regions were impacted by multiple MVs and TSVs. However, in some cases, individual DOW-documented TSV passages can be linked to tornadolike damage swaths. One particularly intense and persistent TSV was tracked as it moved southeastward, west of Rockport (Fig. 7). Damage to a variety of structures [damage indicators (DIs)] visible in aerial surveys (Google Earth and NOAA 2017) was categorized using enhanced Fujita scale (EF) degrees of damage (DoD) and implied 3-s wind speeds up to 55–60 m s^{-1} (WSEC 2006). These inferred peak wind gusts were similar to, but slightly lower than, the maximum winds observed at the DOW, probably because this TSV was between MVs. Interpretation of the wind speeds resulting in damage are complicated by unobserved variations in construction quality. The Doppler wind speed perturbation in this TSV was strongest ($\pm$20 m s^{-1}) near the areas of the most severe damage near the coast. Enhanced winds caused by TSVs and MVs likely caused increases in damage potential from the background near-surface wind speed of 39 m s^{-1} (DOW-anemometer average during passage of eyewall). These increased wind gusts range from those consistent with EF-1 (e.g., minor roof damage to residential structures) to EF-2/3 (e.g., major structural damage and speeds of 60–65 m s^{-1} such as observed near the DOW). Unlike what is typical in tornadoes, this damage swath is superimposed on a broad region of background damage, making it less distinct. DOW data revealed other weaker TSVs crossing north of the strongest TSV, and these are likely responsible for additional damage adjacent to the main swath, near the coast. These observations and analysis represent the first documentation and mapping of TSVs likely responsible for some of the most severe localized damage.

Severe damage, suggestive of the occurrence of some of the strongest wind speeds during Harvey's landfall, occurred 350 m north of the DOW. Three sport utility vehicles (SUVs) parked inside a destroyed building were lofted (Fig. 7), likely by the MV-embedded TSV, which caused the 65 m s^{-1} gust measured at the DOW. The wind direction measured by the DOW anemometer during intensified winds caused by mesocyclone passages was typically from 350° to 360°, implying that the

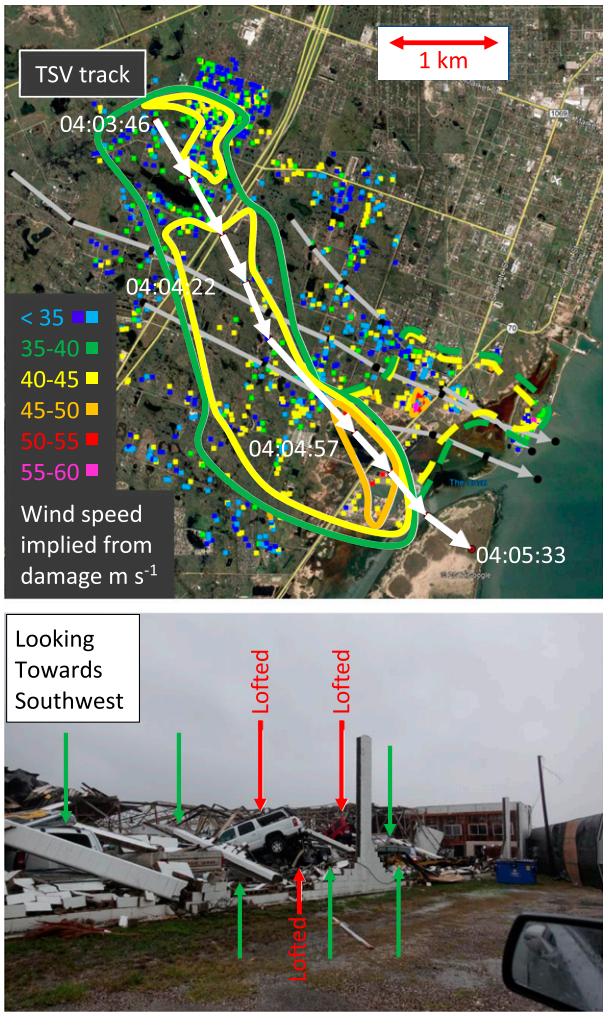

FIG. 7. Damage likely caused by an intense TSV. (top) Wind speeds implied by damage along the track of an intense TSV. Track of center of TSV as measured by DOW (white line); indicated times are indicated in HH:MM:SS UTC. Paths of other, weaker, TSVs indicated with gray lines. Contours outline areas where damage above various thresholds was common. Dashed contours enclose damage likely caused by other TSVs. (bottom) Vehicles lofted (red arrows) and not lofted (green arrows) 350 m north of DOW.

portion of the phenomena that caused the gust that lofted the vehicles passed near or over (0–80 m east of) the DOW (350 m)/(65 m s^{-1}) = 5 s later. This is the first-ever proximate field measurement of a wind gust causing vehicles to become airborne.

The use of lofted vehicles to estimate wind speeds is complicated by the rarity of lofting events and the paucity of actual wind measurements near locations where lofting occurs. Field observations and laboratory simulation results are not consistent; thus, comparisons with our current results are necessarily approximate. Laboratory simulations suggest that vehicle lofting

becomes more likely at wind speeds associated with high-end F/EF-3 or low-end F/EF-4 range (~70–95 m s^{-1}) (Schmidlin et al. 2002; Haan et al. 2017), while some field observations indicate that only 15% of vehicles are rolled or lofted within that wind speed range (Paulikas et al. 2016). A Chevrolet Suburban (SUV) containing one of us (Wurman) was parked pointing southward (leeward) 3 m west of the DOW in an open area, fully exposed to the northerly gusts. Fortunately, it was not lofted. Six vehicles near the two lofted vehicles were not lofted (Fig. 7). Depending on whether the Suburban near the DOW is counted, the percentage of vehicles (not including the much heavier DOW) lofted was 33% or 29%. The lofted vehicles were in a less openly exposed area than the DOW or Suburban, better characterized as "roughly open," with a corresponding $z_0 \sim 0.1$ m (Wieringa et al. 2001). This less-open exposure likely resulted in reduced vehicle-level wind speeds, compared to those experienced at the DOW or near the Suburban. Anemometer measurements at 8 m AGL at the DOW site ($z_0 \sim 0.05$ m) can be adjusted to 1 m AGL, resulting in winds of 38 m s^{-1} (35 m s^{-1} 3-s average) at the collocated Suburban and 33 m s^{-1} (31 m s^{-1} 3-s average) at the other vehicles ($z_0 \sim 0.1$ m).

6. Summary

These observations and analyses provide the first direct evidence of the role of MVs and TSVs in modulating measured surface winds and severe damage caused by a hurricane, as well as the first mapping and characterization of TSVs. Understanding the prevalence, occurrence, frequency, propagation speed, intensity, and structure of TSVs and MVs and, importantly, their impact on surface winds and damage is critical for better prediction of the wind hazards associated with landfalling hurricanes. This is particularly important for hurricanes that are intense and/or intensifying near the time of landfall. Not all landfalling hurricanes exhibit MVs. DOWs have been deployed in the eyewalls/eyes of 14 hurricanes (e.g., Wurman and Winslow 1998; Kosiba et al. 2013; Kosiba and Wurman 2014) and observed MV structures in only two, Harvey (2017) and Ike (2008) (Kosiba and Wurman 2010). It is notable that only Ike and Harvey were intensifying at landfall and had vigorously convective eyewall structures, while the others were already weakening prior to landfall, likely due to the effects of nearby land, wind shear, and/or dry air entrainment. It is possible that intensifying hurricanes also are more likely to exhibit TSVs.

TSVs may be rare, as suggested by Krupar et al. (2016) and Giammanco et al. (2016), or may just be infrequently sampled due to the sparsity of finescale surface observations (Nolan et al. 2014).

If TSVs are common, then it is likely that evidence has been present in historic anemometer data (e.g., Schroeder et al. 2002; Masters et al. 2010; Kosiba and Wurman 2010; Giammanco et al. 2016), but not attributed to the previously undocumented TSVs. It may prove valuable to examine DOW and anemometer data and damage mapping from other hurricanes to explore possible TSV occurrence and effects. Comparisons of damage to anemometer-observed winds or radar-observed structures, such as MVs, TSVs, or HBLRs, are difficult, except in the most intense landfalling hurricanes, where a wider dynamic range of wind damage occurs. Real-time visual documentation of damage would be valuable to aid in deconvolving the effects of multiple MVs, TSVs, or HBLRs. Since the frequency of intense hurricanes and rapid intensification just prior to landfalls may increase with climate change (Knutson et al. 2010; Emanuel 2017), these results may be of increasing importance for the understanding and prediction of, and design for resilience against, TSVs, MVs, HBLRs, and related hazards.

Acknowledgments. DOW Facility supported by NSF-AGS-1361237. Analysis supported by NSF-AGS-1759461 and NSF-AGS-1447268. Paul Robinson assisted with much of this analysis.

REFERENCES

Aberson, S., M. T. Montgomery, M. M. Bell, and M. Black, 2006: Hurricane Isabel (2003): New insights into the physics of intense storms. Part II: Extreme localized wind. *Bull. Amer. Meteor. Soc.*, **87**, 1349–1354, https://doi.org/10.1175/BAMS-87-10-1349.

Alexander, C. R., and J. Wurman, 2008: Updated mobile radar climatology of supercell tornado structures and dynamics. *24th Conf. on Severe Local Storms*, Savannah, GA, Amer. Meteor. Soc., 19.4, https://ams.confex.com/ams/pdfpapers/141821.pdf.

Bluestein, H. B., and F. D. Marks, 1987: On the structure of the eyewall of Hurricane Diana (1984): Comparison of radar and visual characteristics. *Mon. Wea. Rev.*, **115**, 2542–2552, https://doi.org/10.1175/1520-0493(1987)115<2542:OTSOTE>2.0.CO;2.

Corbosiero, K. L., J. Molinari, A. R. Aiyyer, and M. L. Black, 2006: The structure and evolution of Hurricane Elena (1985). Part II: Convective asymmetries and evidence for vortex Rossby waves. *Mon. Wea. Rev.*, **134**, 3073–3091, https://doi.org/10.1175/MWR3250.1.

CSWR, 2018: About the DOWs. Center for Severe Weather Research, accessed 3 November 2017, http://www.cswr.org/contents/aboutdows.php.

Dapena, K., D. Hernandez, and A. Campo-Flores, 2017: Inside Puerto Rico's struggle to recover a month after hurricane. *The Wall Street Journal*, accessed 3 November 2017, https://www.wsj.com/articles/inside-puerto-ricos-struggle-to-recover-a-month-after-hurricane-1508491811.

Durst, C. S., 1960: Wind speeds over short periods of time. *Meteor. Mag.*, **89**, 181–186.

Edwards, R., J. G. LaDue, J. T. Ferree, K. Scharfenberg, C. Maier, and W. L. Coulbourne, 2013: Tornado intensity estimation:

Past, present, and future. *Bull. Amer. Meteor. Soc.*, **94**, 641–653, https://doi.org/10.1175/BAMS-D-11-00006.1.

Emanuel, K., 2017: Will global warming make hurricane forecasting more difficult? *Bull. Amer. Meteor. Soc.*, **98**, 495–501, https://doi.org/10.1175/BAMS-D-16-0134.1.

Foster, R. C., 2005: Why rolls are prevalent in the hurricane boundary layer. *J. Atmos. Sci.*, **62**, 2647–2661, https://doi.org/10.1175/JAS3475.1.

Fujita, T. T., 1992: Damage survey of Hurricane Andrew in south Florida. *Storm Data*, **34**, 25–30.

Giammanco, I. M., J. L. Schroeder, F. J. Masters, P. J. Vickery, R. J. Krupar, and J.-A. Balderrama, 2016: Influences on observed near-surface gust factors in landfalling U.S. Gulf Coast hurricanes: 2004–08. *J. Appl. Meteor. Climatol.*, **55**, 2587–2611, https://doi.org/10.1175/JAMC-D-16-0053.1.

Google Earth and NOAA, 2017: Hurricane Harvey imagery. NOAA, https://storms.ngs.noaa.gov/storms/harvey/index.html#7/28.400/-96.690.

Haan, F. L., P. P. Sarkar, G. A. Kopp, and D. A. Stedman, 2017: Critical wind speeds for tornado-induced vehicle movements. *J. Wind Eng. Ind. Aerodyn.*, **168**, 1–8, https://doi.org/10.1016/j.jweia.2017.04.014.

Hendricks, E. A., B. D. McNoldy, and W. H. Schubert, 2012: Observed inner-core structural variability in Hurricane Dolly (2008). *Mon. Wea. Rev.*, **140**, 4066–4077, https://doi.org/10.1175/MWR-D-12-00018.1.

Irfan, U., 2017: The stunning price tags for Hurricanes Harvey and Irma, explained. Vox, accessed 3 November 2017, https://www.vox.com/explainers/2017/9/18/16314440/disasters-are-getting-more-expensive-harvey-irma-insurance-climate.

Ito, J., T. Oizumi, and H. Niino, 2017: Near-surface coherent structures explored by large eddy simulation of entire tropical cyclones. *Sci. Rep.*, **7**, 3798, https://doi.org/10.1038/s41598-017-03848-w.

Knutson, T. R., and Coauthors, 2010: Tropical cyclones and climate change. *Nat. Geosci.*, **3**, 157–163, https://doi.org/10.1038/ngeo779.

Kosiba, K. A., and J. Wurman, 2010: Fine-scale radar observations of boundary layer structures in landfalling hurricanes. *25th Conf. on Severe Local Storms*, Denver, CO, Amer. Meteor. Soc., P3.5, https://ams.confex.com/ams/25SLS/techprogram/paper_176031.htm.

——, and ——, 2014: Finescale dual-Doppler analysis of hurricane boundary layer structures in Hurricane Frances (2004) at landfall. *Mon. Wea. Rev.*, **142**, 1874–1891, https://doi.org/10.1175/MWR-D-13-00178.1.

——, ——, F. J. Masters, and P. Robinson, 2013: Mapping of near-surface winds in Hurricane Rita using finescale radar, anemometer, and land-use data. *Mon. Wea. Rev.*, **141**, 4337–4349, https://doi.org/10.1175/MWR-D-12-00350.1.

Kossin, J. P., and W. H. Schubert, 2001: Mesovortices, polygonal flow patterns, and rapid pressure falls in hurricane-like vortices. *J. Atmos. Sci.*, **58**, 2196–2209, https://doi.org/10.1175/1520-0469(2001)058<2196:MPFPAR>2.0.CO;2.

——, and ——, 2004: Mesovortices in Hurricane Isabel. *Bull. Amer. Meteor. Soc.*, **85**, 151–153, https://doi.org/10.1175/BAMS-85-2-151.

Krupar, R. J., J. L. Schroeder, D. A. Smith, S.-L. Kang, and S. Lorsolo, 2016: A comparison of ASOS near-surface winds and WSR-88D-derived wind speed profiles measured in landfalling tropical cyclones. *Wea. Forecasting*, **31**, 1343–1361, https://doi.org/10.1175/WAF-D-15-0162.1.

Lee, W. C., and J. Wurman, 2005: Diagnosed three-dimensional axisymmetric structure of the Mulhall tornado on 3 May 1999. *J. Atmos. Sci.*, **62**, 2373–2393, https://doi.org/10.1175/JAS3489.1.

Lorsolo, S., J. L. Schroeder, P. Dodge, and F. D. Marks Jr., 2008: An observational study of hurricane boundary layer small-scale coherent structures. *Mon. Wea. Rev.*, **136**, 2871–2893, https://doi.org/10.1175/2008MWR2273.1.

——, J. A. Zhang, F. D. Marks Jr., and J. Gamache, 2010: Estimation and mapping of hurricane turbulent energy using airborne Doppler measurements. *Mon. Wea. Rev.*, **138**, 3656–3670, https://doi.org/10.1175/2010MWR3183.1.

Marks, F. D., P. G. Black, M. T. Montgomery, and R. W. Burpee, 2008: Structure of the eye and eyewall of Hurricane Hugo (1989). *Mon. Wea. Rev.*, **136**, 1237–1259, https://doi.org/10.1175/2007MWR2073.1.

Masters, F. J., H. W. Tieleman, and J. A. Balderrama, 2010: Surface wind measurements in three Gulf Coast hurricanes of 2005. *J. Wind Eng. Ind. Aerodyn.*, **98**, 533–547, https://doi.org/10.1016/j.jweia.2010.04.003.

McCaul, E. W., D. E. Buechler, S. J. Goodman, and M. Cammarata, 2004: Doppler radar and lightning network observations of a severe outbreak of tropical cyclone tornadoes. *Mon. Wea. Rev.*, **132**, 1747–1763, https://doi.org/10.1175/1520-0493(2004)132<1747:DRALNO>2.0.CO;2.

Montgomery, M. T., and R. J. Kallenbach, 1997: A theory for vortex Rossby-waves and its application to spiral bands and intensity changes in hurricanes. *Quart. J. Roy. Meteor. Soc.*, **123**, 435–465, https://doi.org/10.1002/qj.49712353810.

——, V. A. Vladimirov, and P. V. Denissenko, 2002: An experimental study on hurricane mesovortices. *J. Fluid Mech.*, **471**, 1–32, https://doi.org/10.1017/S0022112002001647.

——, M. M. Bell, S. Aberson, and M. Black, 2006: Hurricane Isabel (2003): New insights into the physics of intense storms. Part I: Mean vortex structure and maximum intensity estimates. *Bull. Amer. Meteor. Soc.*, **87**, 1335–1347, https://doi.org/10.1175/BAMS-87-10-1335.

Morrison, I., S. Businger, F. Marks, P. Dodge, and J. A. Businger, 2005: An observational case for the prevalence of roll vortices in the hurricane boundary layer. *J. Atmos. Sci.*, **62**, 2662–2673, https://doi.org/10.1175/JAS3508.1.

NCAR, 2018: NCAR Command Language, version 6.4.0. UCAR, https://doi.org/10.5065/D6WD3XH5.

Nolan, D. S., J. A. Zhang, and E. W. Uhlhorn, 2014: On the limits of estimating the maximum wind speeds in hurricanes. *Mon. Wea. Rev.*, **142**, 2814–2837, https://doi.org/10.1175/MWR-D-13-00337.1.

Paulikas, M. J., T. W. Schmidlin, and T. P. Marshall, 2016: The stability of passenger vehicles at tornado wind intensities of the (enhanced) Fujita scale. *Wea. Climate Soc.*, **8**, 85–91, https://doi.org/10.1175/WCAS-D-15-0051.1.

Reasor, P. D., M. D. Eastin, and J. F. Gamache, 2009: Rapidly intensifying Hurricane Guillermo (1997). Part I: Low-wavenumber structure and evolution. *Mon. Wea. Rev.*, **137**, 603–631, https://doi.org/10.1175/2008MWR2487.1.

Rogers, R., S. Lorsolo, P. Reasor, J. Gamache, and F. Marks, 2012: Multiscale analysis of tropical cyclone kinematic structure from airborne Doppler radar composites. *Mon. Wea. Rev.*, **140**, 77–99, https://doi.org/10.1175/MWR-D-10-05075.1.

Schmidlin, T. W., B. Hammer, P. King, Y. Ono, L. S. Miller, and G. Thumann, 2002: Unsafe at any (wind) speed?: Testing the stability of motor vehicles in severe winds. *Bull. Amer. Meteor. Soc.*, **83**, 1821–1830, https://doi.org/10.1175/BAMS-83-12-1821.

Schroeder, J. L., and D. A. Smith, 2003: Hurricane Bonnie wind flow characteristics as determined from WEMITE. *J. Wind*

Eng. Ind. Aerodyn., **91**, 767–789, https://doi.org/10.1016/S0167-6105(02)00475-0.

——, M. R. Conder, and J. R. Howard, 2002: Additional insights into hurricane gust factors. Preprints, *25th Conf. on Hurricanes and Tropical Meteorology*, San Diego, CA, Amer. Meteor. Soc., P1.25, https://ams.confex.com/ams/25HURR/techprogram/paper_36949.htm.

Spratt, S. M., D. W. Sharp, P. Welsh, A. Sandrik, F. Alsheimer, and C. Paxton, 1997: A WSR-88D assessment of tropical cyclone outer rainband tornadoes. *Wea. Forecasting*, **12**, 479–501, https://doi.org/10.1175/1520-0434(1997)012<0479:AWAOTC>2.0.CO;2.

Stern, D. P., G. H. Bryan, and S. D. Aberson, 2016: Extreme low-level updrafts and wind speeds measured by dropsondes in tropical cyclones. *Mon. Wea. Rev.*, **144**, 2177–2204, https://doi.org/10.1175/MWR-D-15-0313.1.

Stewart, S. R., and S. W. Lyons, 1996: A WSR-88D radar view of Tropical Storm Ed. *Wea. Forecasting*, **11**, 115–135, https://doi.org/10.1175/1520-0434(1996)011<0115:AWRVOT>2.0.CO;2.

Wakimoto, R. M., and P. G. Black, 1994: Damage survey of Hurricane Andrew and its relationship to the eyewall. *Bull. Amer. Meteor. Soc.*, **75**, 189–200, https://doi.org/10.1175/1520-0477(1994)075<0189:DSOHAA>2.0.CO;2.

Wieringa, J., A. Davenport, C. S. B. Grimmond, and T. R. Oke, 2001: New revision of Davenport roughness classification. *Proc. Third European and African Conf. on Wind Engineering*, Eindhoven, Netherlands, IAWE, 8 pp.

Willoughby, H. E., and P. G. Black, 1996: Hurricane Andrew in Florida: Dynamics of a disaster. *Bull. Amer. Meteor. Soc.*, **77**, 543–549, https://doi.org/10.1175/1520-0477(1996)077<0543:HAIFDO>2.0.CO;2.

Wingo, S. M., and K. R. Knupp, 2016: Kinematic structure of mesovortices in the eyewall of Hurricane Ike (2008) derived from ground-based dual-Doppler analysis. *Mon. Wea. Rev.*, **144**, 4245–4263, https://doi.org/10.1175/MWR-D-16-0085.1.

WSEC, 2006: A recommendation for an enhanced Fujita scale (EF-Scale). Texas Tech University Wind Science and Engineering Center Tech. Rep., 95 pp., http://www.spc.noaa.gov/faq/tornado/ef-ttu.pdf.

Wurman, J., 2002: The multiple-vortex structure of a tornado. *Wea. Forecasting*, **17**, 473–505, https://doi.org/10.1175/1520-0434(2002)017<0473:TMVSOA>2.0.CO;2.

——, and J. Winslow, 1998: Intense sub-kilometer-scale boundary layer rolls observed in Hurricane Fran. *Science*, **280**, 555–557, https://doi.org/10.1126/science.280.5363.555.

——, and K. Kosiba, 2013: Finescale radar observations of tornado and mesocyclone structures. *Wea. Forecasting*, **28**, 1157–1174, https://doi.org/10.1175/WAF-D-12-00127.1.

——, J. Straka, E. Rasmussen, M. Randall, and A. Zahrai, 1997: Design and deployment of a portable, pencil-beam, pulsed, 3-cm Doppler radar. *J. Atmos. Oceanic Technol.*, **14**, 1502–1512, https://doi.org/10.1175/1520-0426(1997)014<1502:DADOAP>2.0.CO;2.

——, P. Robinson, C. Alexander, and Y. Richardson, 2007: Low-level winds in tornadoes and potential catastrophic tornado impacts in urban areas. *Bull. Amer. Meteor. Soc.*, **88**, 31–46, https://doi.org/10.1175/BAMS-88-1-31.

——, K. Kosiba, and P. Robinson, 2013: In situ, Doppler radar, and video observations of the interior structure of a tornado and the wind–damage relationship. *Bull. Amer. Meteor. Soc.*, **94**, 835–846, https://doi.org/10.1175/BAMS-D-12-00114.1.

——, ——, ——, and T. Marshall, 2014: The role of multiple-vortex tornado structure in causing storm researcher fatalities. *Bull. Amer. Meteor. Soc.*, **95**, 31–45, https://doi.org/10.1175/BAMS-D-13-00221.1.

Zhu, P., 2008: Impact of land-surface roughness on surface winds during hurricane landfall. *Quart. J. Roy. Meteor. Soc.*, **134**, 1051–1057, https://doi.org/10.1002/qj.265.